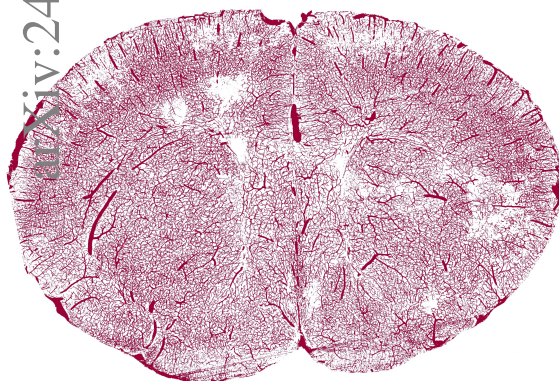


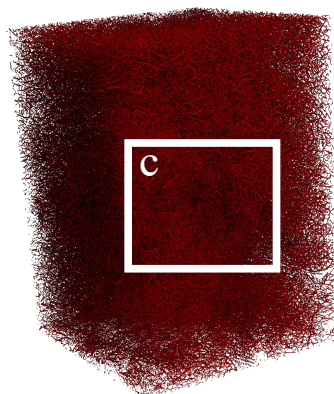
Graphical Abstract

GPU Accelerated RSF Level Set Evolution for Large-Scale Microvascular Segmentation

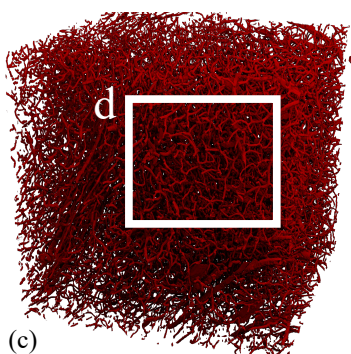
Meher Niger, Helya Goharbavang, Taeyong Ahn, Emily K. Alley, Joshua D. Wylie, Guoning Chen, David Mayerich



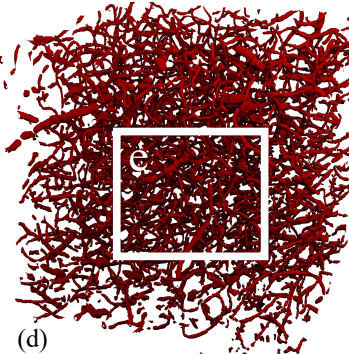
(a) Maximum Intensity Projection of KESM data



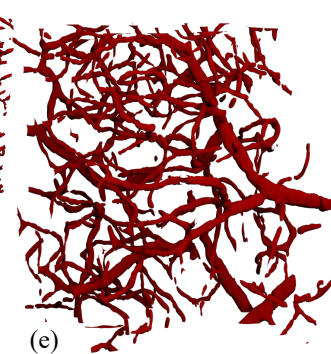
(b) $4000 \times 2000 \times 2000$ voxel



(c)



(d)



(e)

Highlights

GPU-Accelerated RSF Level Set Evolution for Large-Scale Microvascular Segmentation

Meher Niger, Helya Goharbavang, Taeyong Ahn, Emily K. Alley, Joshua D. Wythe, Guoning Chen, David Mayerich

- Reformulation of the Region-Scalable Fitting (RSF) level set model for SIMD and SPMD parallelism
- Demonstration segmenting images of microvascular networks that are extremely large and topologically complex

GPU-Accelerated RSF Level Set Evolution for Large-Scale Microvascular Segmentation

Meher Niger^a, Helya Goharbavang^a, Taeyong Ahn^b, Emily K. Alley^b,
Joshua D. Wythe^{b,c,d,e,f}, Guoning Chen^a, David Mayerich^a

^a*Electrical and Computer Engineering, University of Houston, 4226 Martin Luther King Boulevard, Houston, 77204, TX, United States*

^b*Department of Cell Biology, University of Virginia School of Medicine, Charlottesville, VA, USA*

^c*Department of Neuroscience, University of Virginia School of Medicine, Charlottesville, VA, USA*

^d*Robert M. Berne Cardiovascular Research Center, University of Virginia School of Medicine, Charlottesville, VA, USA*

^e*Brain, Immunology, and Glia (BIG) Center, University of Virginia School of Medicine, Charlottesville, VA, USA*

^f*UVA Comprehensive Cancer Center, University of Virginia School of Medicine, Charlottesville, VA, USA*

Abstract

Microvascular networks are challenging to model because these structures are currently near the diffraction limit for most advanced three-dimensional imaging modalities, including confocal and light sheet microscopy. This makes semantic segmentation difficult, because individual components of these networks fluctuate within the confines of individual pixels. Level set methods are ideally suited to solve this problem by providing surface and topological constraints on the resulting model, however these active contour techniques are extremely time intensive and impractical for terabyte-scale images. We propose a reformulation and implementation of the region-scalable fitting (RSF) level set model that makes it amenable to three-dimensional evaluation using both single-instruction multiple data (SIMD) and single-program multiple-data (SPMD) parallel processing. This enables evaluation of the level set equation on independent regions of the data set using graphics processing units (GPUs), making large-scale segmentation of high-resolution networks practical and inexpensive.

We tested this 3D parallel RSF approach on multiple data sets acquired

using state-of-the-art imaging techniques to acquire microvascular data, including micro-CT, light sheet fluorescence microscopy (LSFM) and milling microscopy. To assess the performance and accuracy of the RSF model, we conducted a Monte-Carlo-based validation technique to compare results to other segmentation methods. We also provide a rigorous profiling to show the gains in processing speed leveraging parallel hardware. This study showcases the practical application of the RSF model, emphasizing its utility in the challenging domain of segmenting large-scale high-topology network structures with a particular focus on building microvascular models.

Keywords: level sets, microscopy, vascular, segmentation

PACS: 0000, 1111

2000 MSC: 0000, 1111

Microvascular networks play a critical role in tissue regulation and disease progression, however their three-dimensional microstructure is poorly understood. This is largely due to limitations in traditional 3D imaging methods, which lack the resolution to fully reconstruct vessels smaller than $10\ \mu\text{m}$ in diameter for large tissue blocks. As advances in light-sheet [1] and milling microscopy [2] improve resolution and acquisition rates, the bottleneck is increasingly shifting to a lack of robust algorithms to build network models from these images.

Most vascular segmentation techniques are designed for large vessels imaged *in vivo* using retinal fundus imaging, magnetic resonance imaging (MRI), and micro-computed tomography (micro-CT) [3, 4]. Open source software for studying microvessel morphology, such as VesselVio [5] and TubeMap [6, 7], rely on a segmentation pipeline that is challenging to optimize because microvessel diameters ($\approx 3\ \mu\text{m}$ to $10\ \mu\text{m}$) are near the current resolution limits of most 3D fluorescent microscopes. Individual microvessels also form complex interconnected networks that span whole organs [8]. The structural complexity, combined with these resolution requirements, makes segmentation algorithms highly sensitive to noise and other artifacts.

Filtering methods such as the Hessian-based *vesselness* filter have been proposed [9] and continuously improved [10] to enhance vessel contrast. However even minor changes in intensity and contrast across a large volume have a significant impact on segmentation accuracy. Semantic segmentation leveraging deep neural networks to enhance contrast have also been explored [11], however these are difficult to generalize and fail to accurately reconstruct

the vessel surface at sub-pixel accuracy. However, applying pre-trained filters (such as convolutional neural networks) to microvascular images may provide effective pre-processing for the proposed active contour approach.

Active contour models such as level sets [12] can take advantage of known structural features, such as interconnectivity and the shape of vessel cross-sections. Region-based force terms [13] are extremely robust in noisy and low-contrast data, providing the potential for a more consistent and deterministic segmentation.

However, these methods are computationally intensive and come with certain limitations. The vast majority focus on two-dimensional segmentation. While three-dimensional approaches have been studied in recent years [14, 15, 16, 17], they are only demonstrated on very low-resolution images acquired using MRI and micro-CT.

To address the computational challenges of existing level set models, we provide a formulation of the state-of-the-art region scalable fitting (RSF) model for three dimensions that enables highly-parallel execution. We also develop a seed surface method for initialization and demonstrate the scalability and accuracy of this approach on a 16GB microvascular image acquired using knife-edge scanning microscopy (KESM) [18, 19].

1. Level Set Method

Level set methods are a mathematical framework for tracking contours across uniform grids, such as two- and three-dimensional images. The distance to a contour is stored at each grid point $\phi(\mathbf{x})$ [20]. The contour evolves over time by calculating the partial derivative $\frac{\delta\phi}{\delta t}$ and using it to update ϕ . At any time t , the embedded surface is reconstructed by finding the isocontour Ω where $\Omega \in \phi(\mathbf{x}) = 0$. The level set function ϕ is usually represented using a signed distance function, where $\phi(\mathbf{x}) < 0$ inside of Ω , which enforces topological consistency and facilitates finding the isocontour Ω .

The contour is moved over discrete time steps t_n by calculating the gradient with respect to time and updating ϕ :

$$\phi_{n+1} = \phi_n + \Delta_t E(\phi, \dots) \tag{1}$$

where

- ϕ_n is the level set function at the current time step n

- ϕ_{n+1} is the updated level set
- Δ_t is the time step
- $E(\phi, \dots)$ is an energy function defining how the contour changes over time

The update function E can be thought of as the partial derivative of ϕ with respect to t . A level set method calculates E to accomplish a desired goal, such as image segmentation. Common components of E include regularization, smoothing, and force terms:

$$E(\phi, \dots) = R(\phi) + \alpha S(\phi) + \beta F(\dots) \quad (2)$$

where α , and β are constants defining the proportional contribution of each term.

1.1. Regularization

The regularization term ensures that ϕ maintains its characteristic as a signed distance function. Without regularization, level set functions exhibit rapid growth on both sides of the contour [21], leading to unexpected movement and discontinuities. Early methods to address this problem rely on periodic reinitialization [22] by calculating a new signed distance function using Fast Sweeping [23] or Fast Marching [24]. However, re-initialization is time-consuming and therefore only used periodically, leading to discontinuities in ϕ over time.

Regularization terms are integrated into the energy function and penalize deviations from $|\nabla\phi| = 1$ to maintain a signed distance field [25]. Li et al. [25] proposed a regularization term to avoid the reinitialization of the level set function, while Wu et al. [26] introduced an extra regularization term for the edge-based level set method.

We employed forward and backward (FAB) diffusion ϕ [13], which has historically good performance for region-based evolution [14, 27].

$$R(\phi) = \nabla^2 \phi - \frac{\nabla^2 \phi}{|\nabla \phi|} \quad (3)$$

1.2. Smoothing

The smoothing term creates an *elastic* effect that minimizes the length or surface area of the contour Ω by penalizing regions of high curvature [13]:

$$S(\phi) = \frac{\nabla^2 \phi}{|\nabla \phi|} \quad (4)$$

This term provides one of the major advantages of level set segmentation over other semantic approaches by fitting a smooth sub-diffraction surface to the image.

1.3. Force

The final term defines a force applied to the contour to achieve a desired goal such as image segmentation. Force terms fall into two categories: (1) edge-based and (2) region-based. Edge-based approaches apply a force to the contour based on its proximity to an edge. An *edge stop function* is often used to slow the contour in the presence of a local edge. This can be approximated using the local gradient [28], edge detection (Insight Toolkit) [29], or statistically-based methods that are more robust to noise [15].

More recent work suggests that region-based approaches exhibit better performance [17] in segmenting objects with complex boundaries. The earliest region-based approaches include work by Chan and Vese [30] that minimize an integral across the interior and exterior of Ω . However, this model faces challenges when the internal or external intensities are not homogeneous.

Region Scalable Fitting (RSF) [13] was proposed to overcome these challenges by integrating across two fitting functions that regionally estimate pixel values on either side of Ω . These fitting functions capture the local mean intensity values adjacent to the contour. More recent advances attempt to capture highly heterogeneous structures using clustering [31] or statistically-based (Gaussian) approaches [32]. The current state-of-the-art, Local Approximation of Taylor Expansion (LATE) [33], extends RSF using a first-order polynomial approximation to the interior intensity.

However, internal heterogeneities are not a major challenge for microvascular models, which have a high surface-to-volume ratio. We therefore build directly on the more fundamental RSF model to take advantage of speed. We provide a detailed explanation of RSF along with a novel generalization to higher dimensions in Section 2.

1.4. Large-Scale Data

Yang et al. proposed a 3D level set method based on RSF to segment low-topology structures in low-resolution brain MR images. Their approach relies on multiple registered atlases to improve the force term [34]. A reaction-diffusion level set method was proposed by Zhang et al. [35] for three-dimensional segmentation on computed tomography (CT) images. These data sets also segment low-topology structures in relatively low resolution ($377 \times 297 \times 306$) images with few artifacts. Another approach using a split Bregman method for medical image segmentation was proposed by Shu et al. [16] for relatively small ($160 \times 160 \times 10$) 3D cardiac MR images. Finally, Zhang et al. introduced a deep learning multi-atlas registration method [36] to achieve a Dice score of 82%. In addition to the required CNN training, the technique also relies on multiple atlases that are unavailable, and likely impossible, for data at cellular resolution.

One of the major challenges with high-resolution 3D microscopy data is the volume size. In addition to parallel segmentation, level set methods may also be amenable to GPU acceleration. A model incorporating YOLOv4 and a region-based active contour model has been proposed by Dlamini et al. [37] for segmenting tumors in $260 \times 260 \times 30$ lung cancer MR images with the Chan and Vese [30] and Mumford Shah [38] models. While implementation details were not provided in the manuscript, these algorithms may be readily parallelized. However, they are sub-optimal when compared to more recent region-based approaches [17].

In this paper, we propose a parallel GPU-based implementation of region-based level sets using RSF as a foundation. We extend RSF to multiple dimensions and describe our approach for an efficient GPU-based implementation. In addition, we provide techniques for seeding and segmentation of gigavoxel 3D microscopy images, including profiling and validation of the segmented results.

2. 3D Region-Scalable Fitting (RSF)

Our proposed approach relies heavily on the RSF model introduced by Li et al. [13]. Our modifications to the theory include (1) extension to higher dimensions ($D > 2$) and (2) a formulation to enable SIMD and SPMD parallelism.

The region-based approach for image segmentation proposed by Chan and Vese [30] calculates the force by minimizing the cost function:

$$C(\Omega, c_-, c_+) = \iint_{\Omega^-} |I(\mathbf{x}) - c_-|^2 d\mathbf{x} + \iint_{\Omega^+} |I(\mathbf{x}) - c_+|^2 d\mathbf{x} \quad (5)$$

across the two regions inside (Ω^-) and outside (Ω^+) of the contour Ω . In this formulation, I is the input image and c_- and c_+ are the average intensities inside and outside of the contour, respectively.

The RSF model [13] modifies these constants into region-based intensities (Figure 1):

$$r_{\pm}(\mathbf{x}) = \frac{K(\sigma_1, \mathbf{x}) * H_{\pm}[\phi(\mathbf{x})] I(\mathbf{x})}{K(\sigma_1, \mathbf{x}) * H_{\pm}[\phi(\mathbf{x})]} \quad (6)$$

where K is an n -dimensional Gaussian kernel:

$$K(\sigma, \mathbf{u}) = \frac{1}{\sqrt{2\pi}\sigma^2} \exp\left[\frac{-\mathbf{u}^T \mathbf{u}}{2\sigma^2}\right] \quad (7)$$

that limits the intensity approximation to pixels in the neighborhood of \mathbf{x} . Similarly, a Heaviside function H_{\pm} limits the contribution to pixels inside or outside of the contour, based on the sign:

$$H_+[\phi(\mathbf{x})] = H_{\epsilon}[\phi(\mathbf{x})] \quad (8)$$

$$H_-[\phi(\mathbf{x})] = 1 - H_{\epsilon}[\phi(\mathbf{x})] \quad (9)$$

A continuous approximation to the Heaviside function is used:

$$H_{\epsilon}(u) = \frac{1}{2} \left[1 + \frac{2}{\pi} \arctan \frac{u}{\epsilon} \right] \quad (10)$$

to avoid division by zero in the denominator of r . A small constant ϵ is used as a regularization term and set based on the numerical precision.

The forces applied in the outward (expanding) and inward (squeezing) directions of the contour are given by:

$$F_{\pm}(\mathbf{x}, r_{\pm}) = \iint_{\Omega^{\pm}} K(\sigma_2, \mathbf{x} - \mathbf{y}) |I(\mathbf{y}) - r_{\pm}(\mathbf{x})|^2 d\mathbf{y} \quad (11)$$

where F_- applies force from the inside of Ω and F_+ applies force from the outside. The final n -dimensional force term is:

$$F(\mathbf{x}, \phi, I) = -[F_+(\mathbf{x}, r_+) - F_-(\mathbf{x}, r_-)] \quad (12)$$

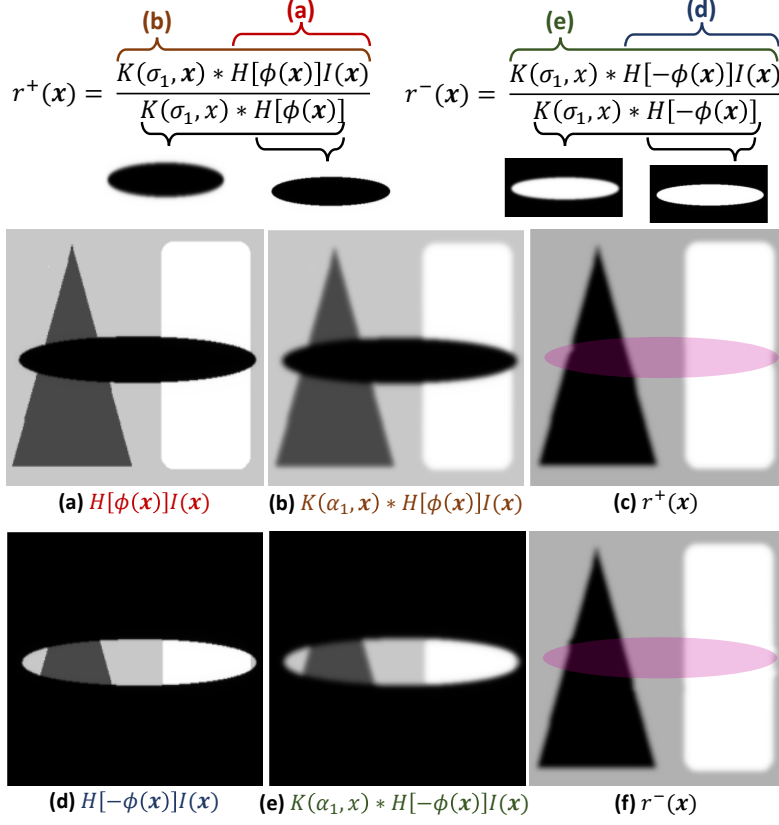


Figure 1: Calculation of the region-based intensities r^+ and r^- . (a, d) The input image is multiplied with the appropriate Heaviside function, and then (b, e) convolved with a Gaussian kernel. (c, f) The final images approximate the local intensity of Ω outside (top) and inside (bottom) of the contour.

Incorporating the smoothing and regularization terms into the level set equation (Equation 2), the final energy function is:

$$E(\phi, I) = \left[\nabla^2 \phi - \frac{\nabla^2 \phi}{|\nabla \phi|} \right] + \delta(\phi) \left(\alpha \left[\frac{\nabla^2 \phi}{|\nabla \phi|} \right] + \beta F(\phi, I) \right) \quad (13)$$

where the impulse function:

$$\delta(u) = \frac{1}{\pi} \frac{\epsilon}{\epsilon^2 + u^2} \quad (14)$$

is the derivative of H_ϵ and constrains the smoothing and force terms to the neighborhood of the contour.

3. Implementation Details

The proposed RSF formulation facilitates parallel computation since the information used to evolve the contour is constrained to the neighborhood of \mathbf{x} by K . This paper leverages two forms of parallelism for large-scale image volumes: *volume level* and *voxel level*. Volume level parallelism breaks the data set into cubic sub-volumes for independent processing. This approach takes advantage of the structure of microvascular networks, where connectivity within the volume is high and interconnections between volumes are localized. Voxel level parallelism takes advantage of SIMD graphics processors (GPUs) by parallelizing the level set calculation and evolution independently at each grid point.

3.1. Volume Level Parallelism

The mesh-like structure of microvessels results in small and highly localized cross-sections when the network is cut by a plane. This provides advantages for parallel contour evolution, since our formulation leverages template calculations for evaluating gradients, curvature, and the local region-based fitting term. Contour cross-sections that cross region boundaries are small and highly localized, making it unlikely for errors to propagate across the contour. In addition, sections are much more likely to occur *across* vessels instead of *along* them, resulting in contours that primarily propagate along the volume boundary where gradient information is more reliable.

Our approach leverages these features by dividing large volumes into manageable 500^3 sub-volumes processed independently on a GPU. Template artifacts are minimized using a curtain region scaled by $\max(\sigma_1, \sigma_2)$.

Neighboring volumes are merged using linear interpolation across the curtain region (Figure 2), which provides the best results when compared to the minimum, maximum, and averaging.

3.2. Voxel Level Parallelism

The directional force (Equation 11) requires two convolutions:

$$F_{\pm}(\mathbf{x}, r_{\pm}) = [K * I^2](\mathbf{x}) - 2r_{\pm}(\mathbf{x})[K * I](\mathbf{x}) + r_{\pm}^2(\mathbf{x}) \quad (15)$$

where K is a separable Gaussian kernel. We decompose the level set evolution terms into independently-evaluated kernels (Figure 3) implemented using CUDA.

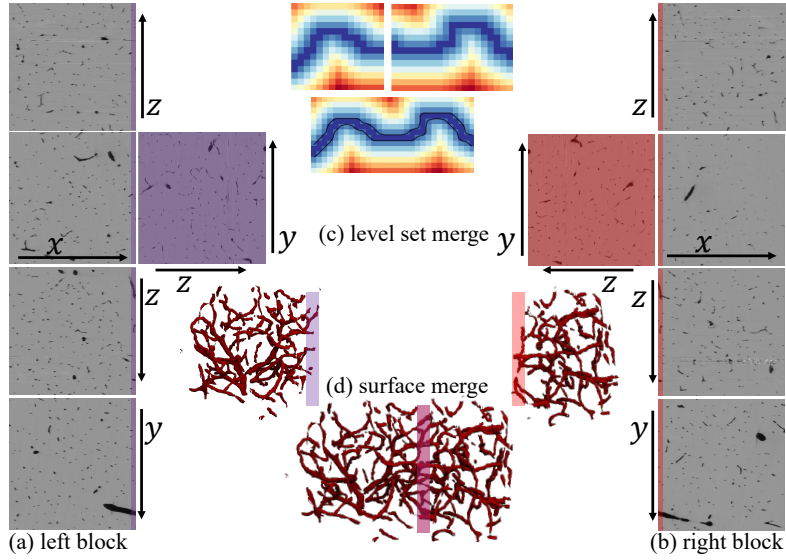


Figure 2: Linear interpolation is used to merge adjacent level set functions (a and b) ϕ_n (c) across overlapping curtain regions (purple/red). The merged ϕ_n is then used to generate the final contour (d).

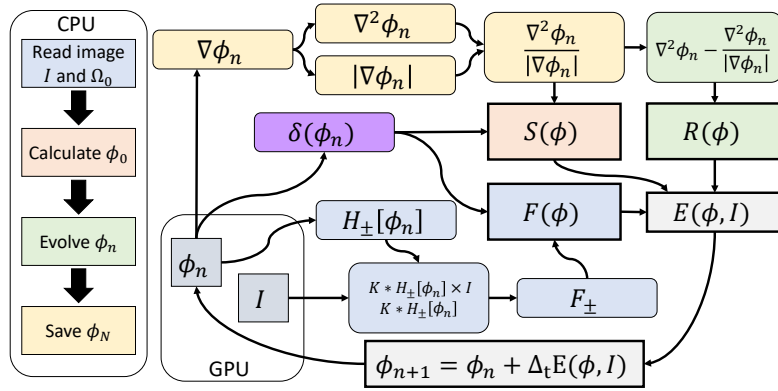


Figure 3: Outline of the proposed 3D RSF algorithm components implemented on the CPU and GPU. The Evolve component is performed completely using CUDA kernels to calculate E , with dependencies listed to minimize redundant computation.

The source image $I(x, y, z)$ and the initial level set ϕ_0 are transferred to the GPU, and all updates occur locally. Iterative updates to ϕ follow two major paths with kernel dependencies shown in Figure 3. Kernels with all satisfied dependencies can be executed on available hardware as resources

permit:

- **$S(\phi)$ and $R(\phi)$ Path:** The gradient kernels are used to calculate the Laplacians for both the smoothing and regularization terms.
- **$F_{\pm}(\phi)$ Path:** The Heaviside functions and associated convolutions with the input image are used to calculate region-based intensities and force terms.

After the smoothing, regularization, and force terms are computed, they are combined into an energy term $E(\phi, I)$ used to update ϕ .

3.3. Initialization

In this section, we present a method for specifying the initial contour by calculating a set of seed points on the network.

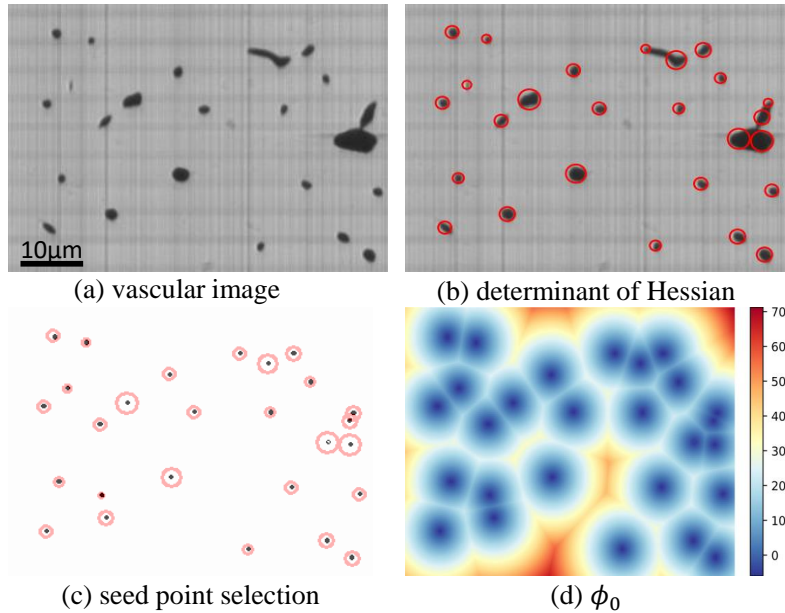


Figure 4: Initializing the level set from an input image (a). Blob detection using the determinant of the Hessian (b) is used to identify candidate seed points (c) on the vascular centerlines. Fast sweeping is then used to determine the positive distance (d) from seed points to create the ϕ_0 .

The determinant of the Hessian matrix blob detection [39] is used to identify a set of candidate seed points \mathbf{S} in each z -axis slice. The level set ϕ_0

is initialized by setting these seed point positions to zero: $\phi_0(\mathbf{x}) = 0$ if $\mathbf{x} \in \mathbf{S}$. ϕ_0 is then initialized to a signed distance function using the fast sweeping algorithm [23].

4. Results

We first demonstrate the proposed RSF formulation on phantom 2D images with varying noise and contrast levels. We then apply the proposed 3D implementation to several types of 3D microscopy capable of imaging large tissue volumes.

4.1. 2D Validation

We first evaluate the performance of the proposed model using 2D synthetic images. While 2D performance has been previously reported [17], our images exhibit interconnected topological features comparable to microvascular networks with contrast and noise variations (Figure 5). The raw image is shown with seed points and the final surface (Figure 5a). Additional images (Figure 5b - 5j) show the level set evolution at intermediate and final time steps for images with various noise and contrast artifacts. Parameter values for all these segmentations were as follows: $\sigma_1 = 19$, $\sigma_2 = 9$, $\beta = 3.5$, $\alpha = 255 \times 255 \times 0.01$ and $dt = 0.1$.

The parameter most sensitive to image noise is σ_1 used to calculate the region-based intensities. However, after testing various combinations, we found that higher values (ex. $\sigma_1 = 19$) were robust for all cases (Figure 6).

4.2. Vascular Image Acquisition

Five comprehensive 3D images of tissue microvasculature were collected using micro-CT (2 brains), light sheet microscopy (brain and ovary), and knife-edge scanning microscopy (brain):

- **Mouse ovary, LSM** (Figure 7): An ovary from a 2-month and 23 days-old female mouse ($BRaf^{V600E/WT}$; $Ai14 R26^{\sigma^{lsl-TdTom/+}}$) perfused with lectin-649 (Vector Laboratories, Product number: DL-1178-1; Newark, CA, USA) and imaged using a Zeiss Z7 (Zeiss, Oberkochen, Baden-Württemberg, Germany) light sheet microscope. The voxel size of the image is $0.949 \mu\text{m} \times 0.949 \mu\text{m} \times 6 \mu\text{m}$, and the file size is 6.6 GB. This image was obtained with 5X lens, 638 nm laser, 18% laser power, 249.67 ms exposure time.

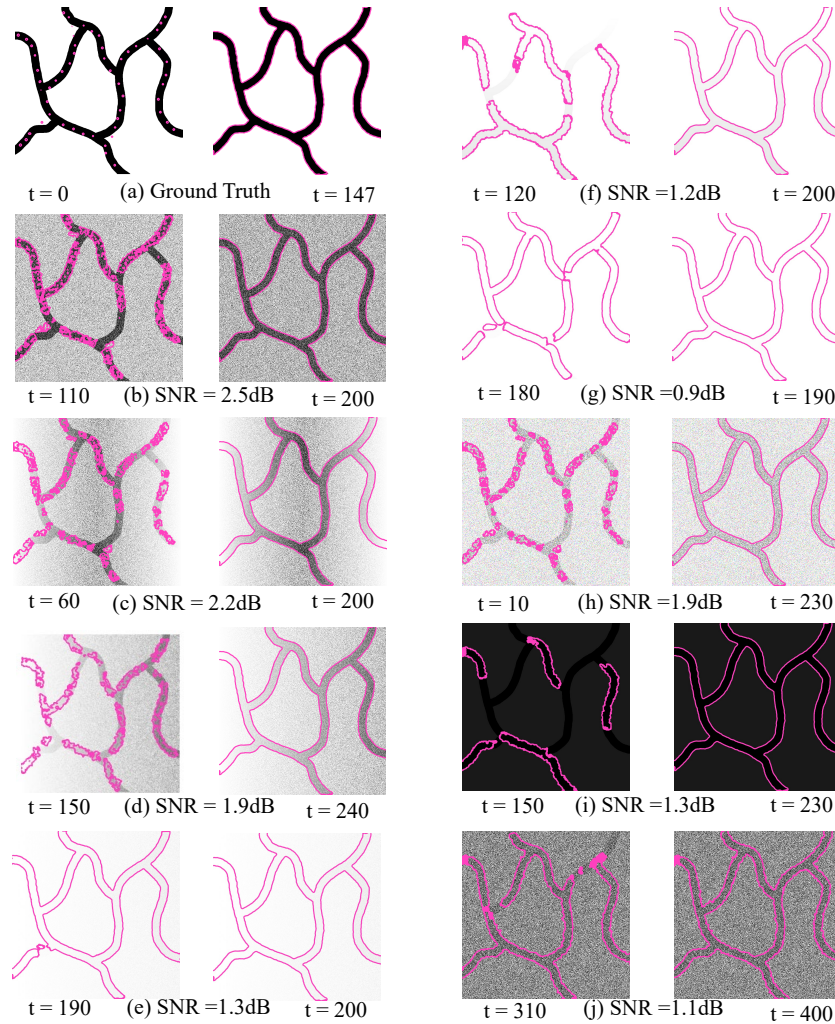


Figure 5: Results of RSF method for 2D synthetic vasculature. The curve evolution process from the initial contour (in the first and third columns) to the final contour (in the second and fourth columns) is shown in every row for the corresponding image. We altered the Signal-to-Noise Ratio (SNR) of the ground truth in certain images through two distinct methods. Firstly, we introduced Gaussian noise, and secondly, we modified the intensity along the x-axis to the y-axis for some images and vice versa along the y-axis to the x-axis for others.

- **Mouse brain, LSM** (Figure 8): A brain from a 4.5-month-old female mouse (C57BL/6N) was perfused with lectin-488 (Vector Laboratories, Product number: DL-1174-1; Newark, CA, USA) and imaged by AxL

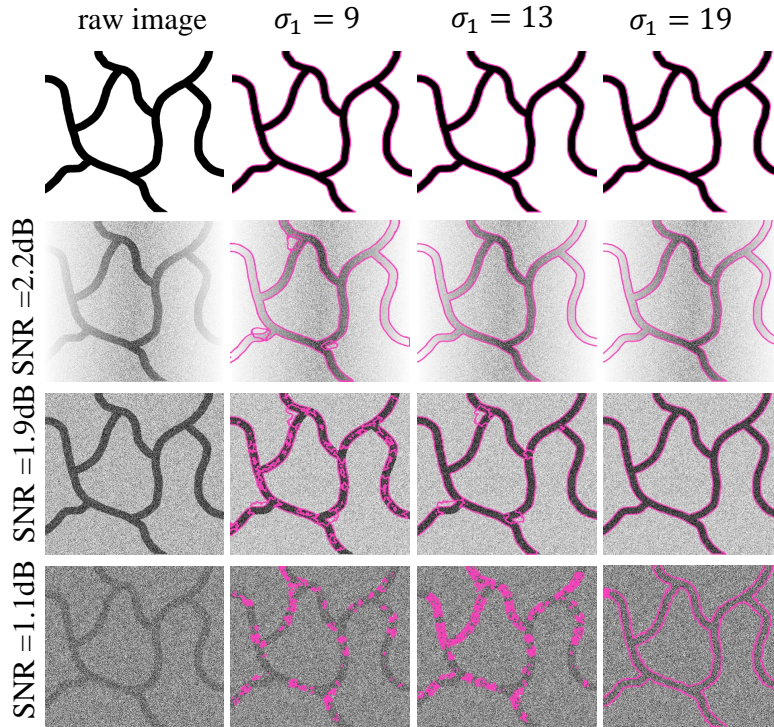


Figure 6: Results of 2D synthetic images for various σ_1 values used to calculate region-based intensities. This demonstrates that the algorithm is insensitive to high σ_1 values for these images.

Cleared Tissue LightSheet (Intelligent Imaging, Denver, CO, USA). The voxel size of the image is $2 \mu\text{m} \times 2 \mu\text{m} \times 6 \mu\text{m}$, and the file size is 103.6 GB. This image was acquired with a 1X lens, 488 nm laser, 200 mW laser power, and 300 ms exposure time.

- **Mouse brain, μ -CT** (Figure 9) Two separate 2 month-old female mouse brains (*Tg(Slco1c1-BAC-CreER); R26^{lsl-TdTom/+}*) were perfused with Vascupaint (MediLumine, Product number: MDL-121; Montreal, Quebec, Canada) and imaged with a Skyscan 1276 (Bruker, Billerica, MA, USA). The imaging was performed at an isotropic voxel size of $10 \mu\text{m}$.
- **Mouse brain, KESM** (Figure 10): Whole mouse mouse brain (C57BL/6J) was perfused with India ink [19] and imaged at a resolution of $0.6 \mu\text{m} \times 0.7 \mu\text{m} \times 1 \mu\text{m}$.

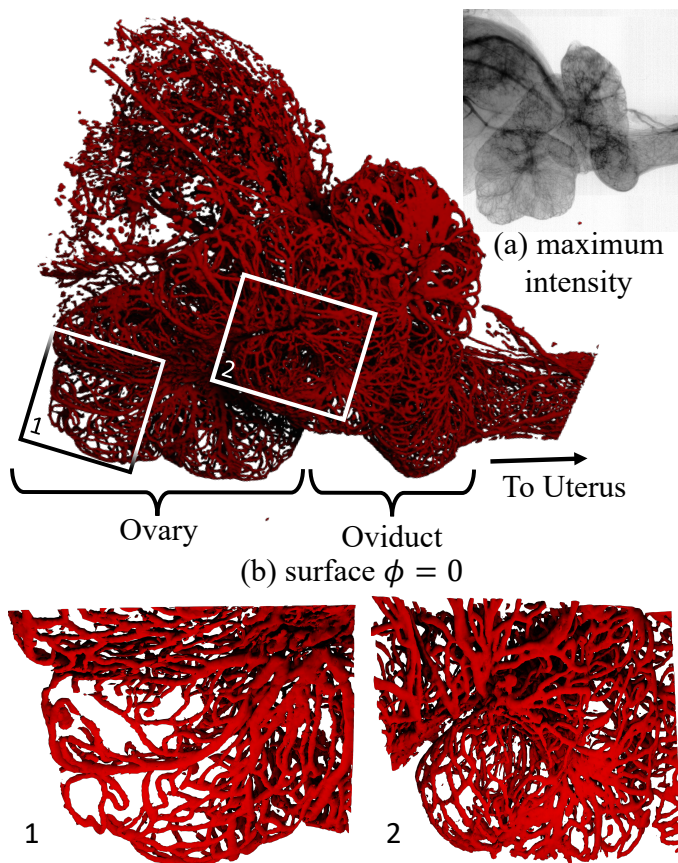


Figure 7: Ovary from a female mouse ($BRaf^{V600E/WT}$) at age 2 months and 23 days. Imaging modality: LSFM, Label: lectin-649, Resolution: $0.949 \mu\text{m} \times 0.949 \mu\text{m} \times 6 \mu\text{m}$, Data size: 6.6 GB. (a) The maximum intensity projection is shown along with (b) the vascular surface where $\phi = 0$. Two labeled insets show magnified regions of the ovary.

4.3. 3D Monte-Carlo Validation

The size and complexity of microvascular networks make extensive manual annotation impractical. To test the viability of the proposed RSF-based level set approach as a segmentation method, we employed Monte-Carlo-based validation.

A randomized set of $100 \times 100 \times 100$ voxel sub-volumes were randomly selected from each image: 13 from KESM, 12 from both CT data sets, and 6 from each LSFM data set. These volumes were manually annotated using 3D Slicer [41] and segmented with the proposed RSF method. Statistics for

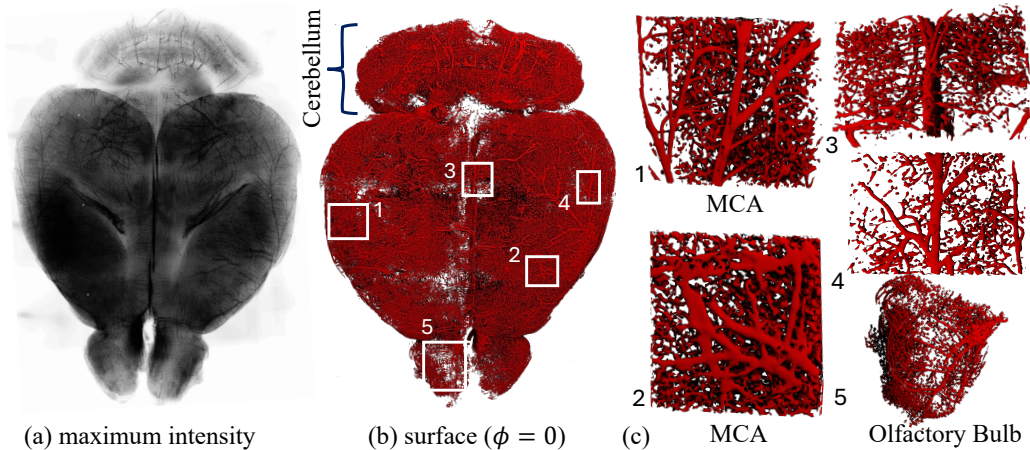


Figure 8: Light sheet microscopy image of a 4.5-month-old female C57BL/6N mouse brain. The vasculature is labeled with a 488 nm fluorescently conjugated tomato lectin. The spatial resolution is $2\ \mu\text{m} \times 2\ \mu\text{m} \times 6\ \mu\text{m}$ with a total data size of 103.6 GB. (a) The maximum intensity projection of the whole brain is shown on the left, with (b) the complete reconstructed network. Cropped magnified regions are shown as magnified insets (c). 1 and 2 show the right and left middle cerebral artery (MCA), and 5 shows the olfactory bulb.

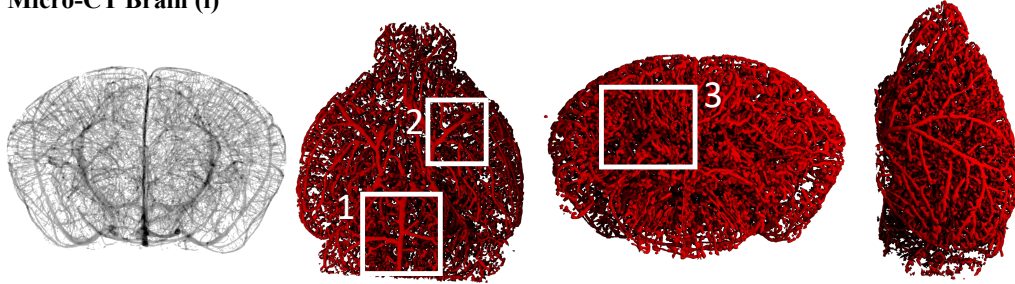
the Dice coefficient [42] and Jaccard index [43] were calculated (Figure 11). All our 3D segmentations used the same parameters for level set evolution: $\sigma_1 = 5$, $\sigma_2 = 0$, $dt = 0.06$, $\alpha = 255 \times 255 \times 0.0009$, $\beta = 0.1$.

RSF results for the LSFM brain image are shown compared to the best-performing alternative (Figure 12), which was Otsu’s method applied to each z-slice section independently. Note that the primary problem is over-segmentation, particularly across the z-axis where the resolution is lowest. This results in the cumulative integration of errors across several sections, as seen in the model visualization (Figure 12(f)).

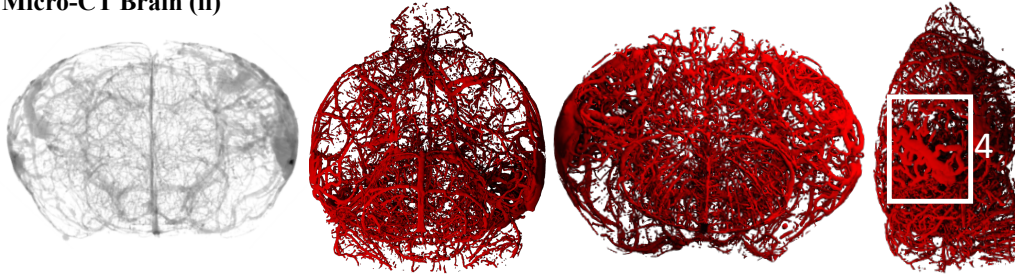
4.4. Performance Profiling

In this section, we present a thorough analysis of the computational performance, focusing on a comparative study between GPU and CPU acceleration. The summarized results of this analysis can be found in Table 1, specifically addressing voxel-level parallelism. Our primary objective is to maximize GPU utilization in order to achieve peak performance. Notably, our GPU model exhibits a significant speedup compared to its CPU counterpart. We have successfully maintained consistent performance across all

Micro-CT Brain (i)



Micro-CT Brain (ii)

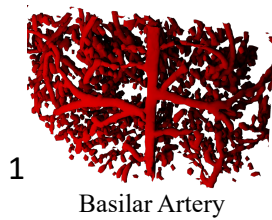


(a) Maximum Intensity

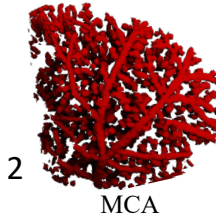
(b) Ventral View

(c) Coronal View

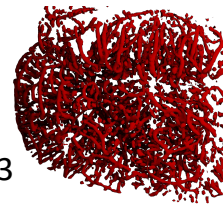
(d) Sagittal View



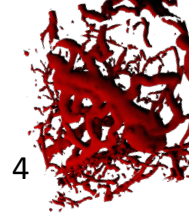
Basilar Artery



MCA



3



4

Figure 9: Two 2-month-old female mouse brains (i) and (ii) with the vasculature perfused with Vascupaint and imaged using a Skyscan 127. The spatial resolution image is $10\ \mu\text{m} \times 10\ \mu\text{m} \times 10\ \mu\text{m}$. (a) Maximum intensity projections are shown along side a (b) ventral view, (c) coronal view, and (d) sagittal view of the reconstructed networks. Cropped magnified regions of these two networks are shown as insets (1-4).

kernels, aligning with our overarching goal.

5. Conclusion

We propose a reformulation of the RSF region-based level set method that is amenable to 3D images and parallel implementation for large data sets. We also provide a GPU-based implementation of this algorithm, including rigorous optimization and profiling for SIMD processors.

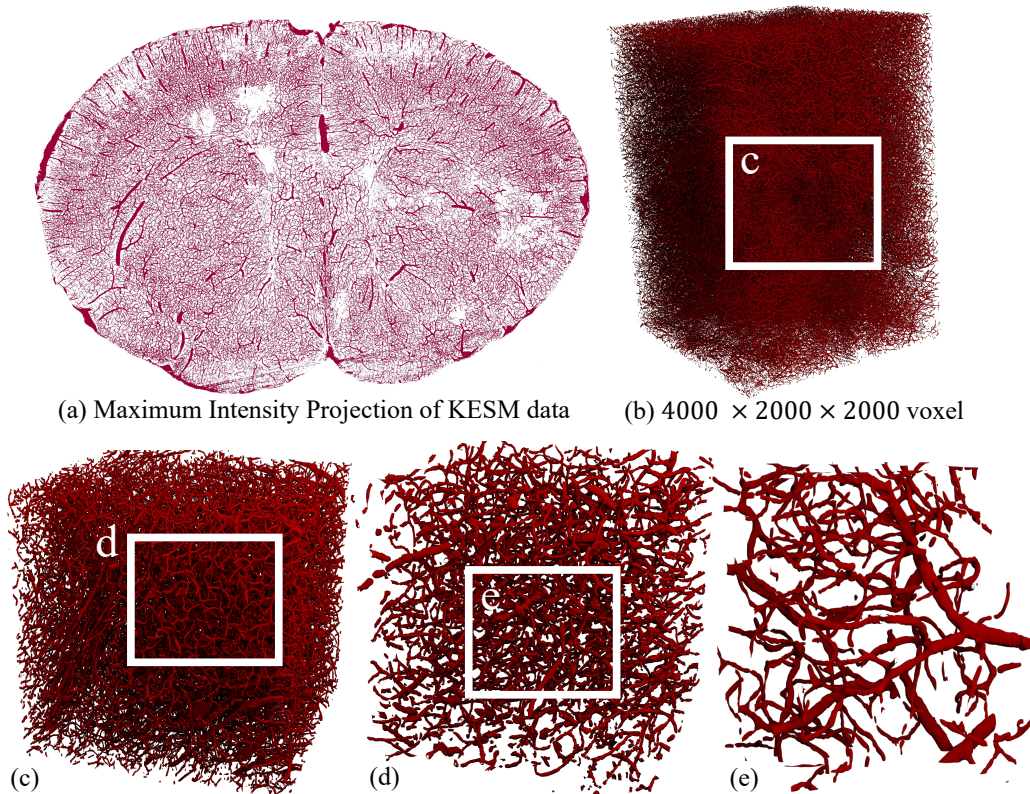


Figure 10: Whole brain vasculature imaged using knife edge scanning microscopy (KESM) and available online (kesm.cs.tamu.edu)[40] and imaged at a resolution of $0.6\ \mu\text{m} \times 0.7\ \mu\text{m} \times 1\ \mu\text{m}$ [19]. (a) Reconstruction from 140 slices across the whole brain is shown, along with (b) a $4000 \times 2000 \times 2000$ voxel sub-volume with (c-e) several iterated higher-resolution zooms.

While the efficacy of RSF has been demonstrated previously on more traditional biomedical images, this is the first demonstration of it on topologically complex structures from emerging microscopy imaging methods. The proposed approach bypasses long computation times and memory requirements by formulating an RSF algorithm that can be applied independently to subvolumes of the whole image and evolved entirely on the GPU.

We also demonstrate a validation method using Monte-Carlo sampling to assess the efficacy of 3D RSF segmentation using the Dice coefficient and Jaccard index. The graphical representations of these comparisons provide compelling evidence of its robustness to noise and contrast changes, as well as its applicability to topologically complex structures.

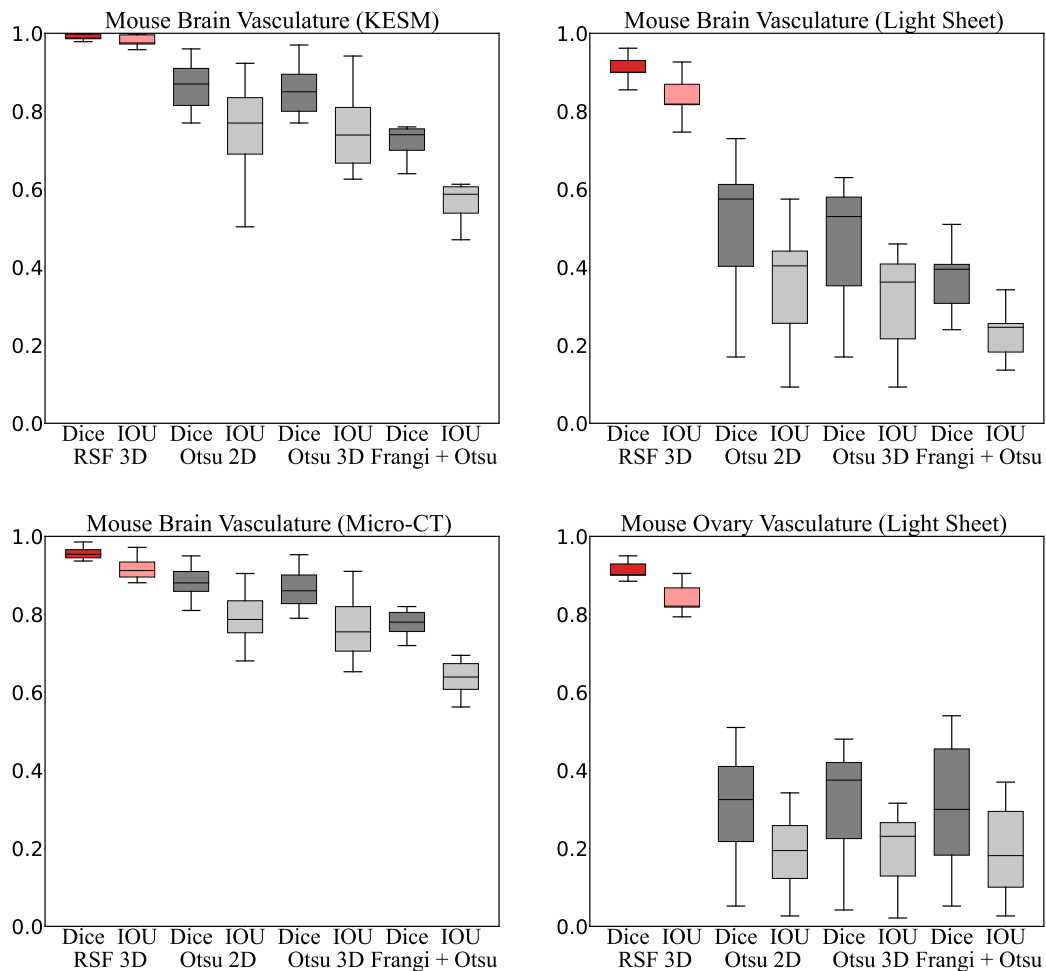


Figure 11: Segmentation results for mouse microvascular networks across modalities. Results are expressed using both the Dice coefficient (dark) and Jaccard index (light). The GPU-based 3D RSF approach proposed here is shown in red. Comparisons use Otsu’s method with and without pre-processing with a vesselness filter [9].

The significance of this work extends beyond the specific implementation of the RSF model by offering a versatile tool for accurate and efficient 3D microvascular segmentation. The integration of GPU acceleration not only improves computational efficiency but also opens new possibilities for large-scale image processing extending to whole organs.

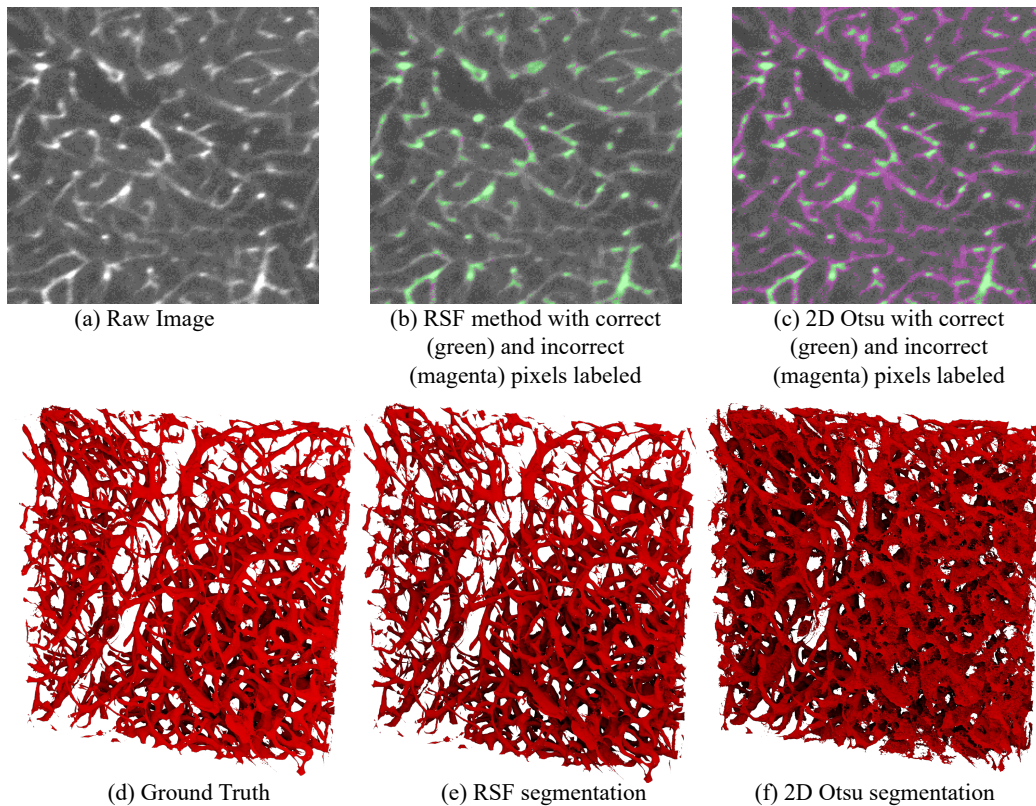


Figure 12: Segmentation results for RSF and Otsu’s method using a 2D ”slice-by-slice” threshold. (a) The raw image is shown with overlays showing correctly labeled pixels (green) with oversegmentation (magenta) using both (b) RSF and (c) Otsu. While the magenta pixels correspond to vessels, they are blurred fluorescence from adjacent slices caused by anisotropic sampling along the z-axis. This results in over-segmentation along the z-axis visible in a 3D visualization of the segmentation results (d-f).

Acknowledgements

This work was supported by grants from the National Institutes of Health to JDW (1R01HL159159) and to JDW and DM (R01HL146745), the National Science Foundation to DM (1943455), as well as generous seed funding from the University of Virginia School of Medicine and UVA Comprehensive Cancer Center to JDW.

DM is a stakeholder in SwiftFront, LLC.

Parameters	GPU	Percent	Speedup
H_-I	41 ms	7.0%	92.6x
H_+I	41 ms	7.0%	92.6x
$K * H_-I$	58 ms	10%	281x
$K * H_+I$	57 ms	9.7%	287x
$K * H_-$	56 ms	9.6%	291x
$K * H_+$	58 ms	10%	282x
$\delta(\nu)$	20 ms	3.4%	165x
$\nabla\phi$	50 ms	8.5%	360x
$ \nabla\phi $	15 ms	2.6%	386x
$\nabla^2\phi$	53 ms	9.1%	358x
$\frac{\nabla\phi}{ \nabla\phi }$	47 ms	8.0%	102x
$\nabla^2\phi - \frac{\nabla\phi}{ \nabla\phi }$	13 ms	2.2%	192x
E_+	38 ms	6.5%	224x
E_-	38 ms	6.5%	224x

Table 1: Profiling on GPU and CPU for a $500 \times 500 \times 500$ voxel. The first column represents the main parameters used in the RSF method. The time required for each time step in GPU is in the second column and in CPU is in the third column. In the fourth column we showed the speeding for each parameter from CPU to GPU.

References

- [1] C.-W. Hsu, J. Cerda III, J. M. Kirk, W. D. Turner, T. L. Rasmussen, C. P. F. Suarez, M. E. Dickinson, J. D. Wythe, Ez clear for simple, rapid, and robust mouse whole organ clearing, *Elife* 11 (2022) e77419.
- [2] G. Knott, H. Marchman, D. Wall, B. Lich, Serial section scanning electron microscopy of adult brain tissue using focused ion beam milling, *Journal of Neuroscience* 28 (12) (2008) 2959–2964.
- [3] N. Heller, F. Isensee, K. H. Maier-Hein, X. Hou, C. Xie, F. Li, Y. Nan, G. Mu, Z. Lin, M. Han, et al., The state of the art in kidney and kidney tumor segmentation in contrast-enhanced ct imaging: Results of the kits19 challenge, *Medical image analysis* 67 (2021) 101821.
- [4] S.-H. Hong, A. M. Herman, J. M. Stephenson, T. Wu, A. N. Bahadur, A. R. Burns, S. P. Marrelli, J. D. Wythe, Development of barium-based low viscosity contrast agents for micro ct vascular casting: Application

to 3d visualization of the adult mouse cerebrovasculature, Tech. rep., Wiley Online Library (2020).

- [5] J. R. Bumgarner, R. J. Nelson, Open-source analysis and visualization of segmented vasculature datasets with vesselvio, *Cell reports methods* 2 (4) (2022).
- [6] N. Renier, E. L. Adams, C. Kirst, Z. Wu, R. Azevedo, J. Kohl, A. E. Autry, L. Kadiri, K. U. Venkataraju, Y. Zhou, et al., Mapping of brain activity by automated volume analysis of immediate early genes, *Cell* 165 (7) (2016) 1789–1802.
- [7] C. Kirst, S. Skriabine, A. Vieites-Prado, T. Topilko, P. Bertin, G. Gerschenfeld, F. Verny, P. Topilko, N. Michalski, M. Tessier-Lavigne, et al., Mapping the fine-scale organization and plasticity of the brain vasculature, *Cell* 180 (4) (2020) 780–795.
- [8] D. Mayerich, J. D. Wythe, Computational insights on coronary artery function, *Nature cardiovascular research* 1 (8) (2022) 691–693.
- [9] A. F. Frangi, W. J. Niessen, K. L. Vincken, M. A. Viergever, Multiscale vessel enhancement filtering, in: *Medical Image Computing and Computer-Assisted Intervention—MICCAI’98: First International Conference Cambridge, MA, USA, October 11–13, 1998 Proceedings 1*, Springer, 1998, pp. 130–137.
- [10] S. Mahapatra, S. Agrawal, P. K. Mishro, R. B. Pachori, A novel framework for retinal vessel segmentation using optimal improved frangi filter and adaptive weighted spatial fcm, *Computers in Biology and Medicine* 147 (2022) 105770.
- [11] L. Saadatfard, A. Mobiny, P. Govyadinov, H. Van Nguyen, D. Mayerich, Cellular/vascular reconstruction using a deep cnn for semantic image preprocessing and explicit segmentation, in: *International Workshop on Machine Learning for Medical Image Reconstruction*, Springer, 2020, pp. 134–144.
- [12] J. A. Sethian, et al., *Level set methods and fast marching methods*, Vol. 98, Cambridge Cambridge UP, 1999.

- [13] C. Li, C.-Y. Kao, J. C. Gore, Z. Ding, Minimization of region-scalable fitting energy for image segmentation, *IEEE transactions on image processing* 17 (10) (2008) 1940–1949.
- [14] Y. Chen, G. Chen, Y. Wang, N. Dey, R. S. Sherratt, F. Shi, A distance regularized level-set evolution model based mri dataset segmentation of brain’s caudate nucleus, *IEEE Access* 7 (2019) 124128–124140.
- [15] C. Liu, W. Liu, W. Xing, A weighted edge-based level set method based on multi-local statistical information for noisy image segmentation, *Journal of Visual Communication and Image Representation* 59 (2019) 89–107.
- [16] X. Shu, Y. Yang, B. Wu, A neighbor level set framework minimized with the split bregman method for medical image segmentation, *Signal Processing* 189 (2021) 108293.
- [17] Z. Wang, B. Ma, Y. Zhu, Review of level set in image segmentation, *Archives of Computational Methods in Engineering* 28 (2021) 2429–2446.
- [18] D. Mayerich, L. Abbott, B. McCormick, Knife-edge scanning microscopy for imaging and reconstruction of three-dimensional anatomical structures of the mouse brain, *Journal of microscopy* 231 (1) (2008) 134–143.
- [19] D. Mayerich, J. Kwon, C. Sung, L. Abbott, J. Keyser, Y. Choe, Fast macro-scale transmission imaging of microvascular networks using kesm, *Biomedical optics express* 2 (10) (2011) 2888–2896.
- [20] S. Osher, J. A. Sethian, Fronts propagating with curvature-dependent speed: Algorithms based on hamilton-jacobi formulations, *Journal of computational physics* 79 (1) (1988) 12–49.
- [21] C. Li, C. Xu, C. Gui, M. D. Fox, Level set evolution without re-initialization: a new variational formulation, in: 2005 IEEE computer society conference on computer vision and pattern recognition (CVPR’05), Vol. 1, IEEE, 2005, pp. 430–436.
- [22] S. Osher, R. P. Fedkiw, *Level set methods and dynamic implicit surfaces*, Vol. 1, Springer New York, 2005.

- [23] H. Zhao, A fast sweeping method for eikonal equations, *Mathematics of computation* 74 (250) (2005) 603–627.
- [24] J. A. Sethian, Fast marching methods, *SIAM review* 41 (2) (1999) 199–235.
- [25] C. Li, C. Xu, C. Gui, M. D. Fox, Distance regularized level set evolution and its application to image segmentation, *IEEE transactions on image processing* 19 (12) (2010) 3243–3254.
- [26] W. Wu, Y. Wu, Q. Huang, An improved distance regularized level set evolution without re-initialization, in: *2012 IEEE Fifth International Conference on Advanced Computational Intelligence (ICACI)*, IEEE, 2012, pp. 631–636.
- [27] X. Wang, J. Shan, Y. Niu, L. Tan, S.-X. Zhang, Enhanced distance regularization for re-initialization free level set evolution with application to image segmentation, *Neurocomputing* 141 (2014) 223–235.
- [28] R. Szeliski, *Computer vision: algorithms and applications*, Springer Nature, 2022.
- [29] T. S. Yoo, *Insight into images: principles and practice for segmentation, registration, and image analysis*, AK Peters Ltd, 2004.
- [30] T. F. Chan, L. A. Vese, Active contours without edges, *IEEE Transactions on image processing* 10 (2) (2001) 266–277.
- [31] H. Min, X.-F. Wang, D.-S. Huang, W. Jia, A novel dual minimization based level set method for image segmentation, *Neurocomputing* 214 (2016) 910–926.
- [32] H. Yu, F. He, Y. Pan, A novel region-based active contour model via local patch similarity measure for image segmentation, *Multimedia Tools and Applications* 77 (2018) 24097–24119.
- [33] H. Min, W. Jia, Y. Zhao, W. Zuo, H. Ling, Y. Luo, Late: A level-set method based on local approximation of Taylor expansion for segmenting intensity inhomogeneous images, *IEEE Transactions on Image Processing* 27 (10) (2018) 5016–5031.

- [34] Y. Yang, W. Jia, Y. Yang, Multi-atlas segmentation and correction model with level set formulation for 3d brain mr images, *Pattern Recognition* 90 (2019) 450–463.
- [35] Z. Zhang, Y. M. Xie, Q. Li, S. Zhou, A reaction–diffusion based level set method for image segmentation in three dimensions, *Engineering Applications of Artificial Intelligence* 96 (2020) 103998.
- [36] Y. Zhang, J. Wu, Y. Liu, Y. Chen, W. Chen, E. X. Wu, C. Li, X. Tang, A deep learning framework for pancreas segmentation with multi-atlas registration and 3d level-set, *Medical Image Analysis* 68 (2021) 101884.
- [37] S. Dlamini, Y.-H. Chen, C.-F. J. Kuo, Complete fully automatic detection, segmentation and 3d reconstruction of tumor volume for non-small cell lung cancer using yolov4 and region-based active contour model, *Expert Systems with Applications* 212 (2023) 118661.
- [38] D. B. Mumford, J. Shah, Optimal approximations by piecewise smooth functions and associated variational problems, *Communications on pure and applied mathematics* (1989).
- [39] X. Xu, Blob detection with the determinant of the hessian, in: *Pattern Recognition: 6th Chinese Conference, CCPR 2014, Changsha, China, November 17-19, 2014. Proceedings, Part I* 6, Springer, 2014, pp. 72–80.
- [40] J. R. Chung, C. Sung, D. Mayerich, J. Kwon, D. E. Miller, T. Huffman, J. Keyser, L. C. Abbott, Y. Choe, Multiscale exploration of mouse brain microstructures using the knife-edge scanning microscope brain atlas, *Frontiers in neuroinformatics* 5 (2011) 29.
- [41] S. Pieper, M. Halle, R. Kikinis, 3d slicer, in: *2004 2nd IEEE international symposium on biomedical imaging: nano to macro (IEEE Cat No. 04EX821)*, IEEE, 2004, pp. 632–635.
- [42] J. M. Duarte, J. B. d. Santos, L. C. Melo, Comparison of similarity coefficients based on rapd markers in the common bean, *Genetics and Molecular Biology* 22 (1999) 427–432.
- [43] R. Real, J. M. Vargas, The probabilistic basis of jaccard’s index of similarity, *Systematic biology* 45 (3) (1996) 380–385.